

A multiconfigurational study of the negatively charged nitrogen-vacancy center in diamond

Churna Bhandari,^{1,*} Aleksander L. Wysocki,¹ Sophia E. Economou,¹ Pratibha Dev,² and Kyungwha Park^{1,†}

¹*Department of Physics, Virginia Tech, Blacksburg, Virginia 24061, USA*

²*Department of Physics and Astronomy, Howard University, Washington, DC 20059, USA*

(Dated: October 13, 2020)

Deep defects in wide band gap semiconductors have emerged as leading qubit candidates for realizing quantum sensing and information applications. Due to the spatial localization of the defect states, these deep defects can be considered as artificial atoms/molecules in a solid state matrix. Here we show that unlike single-particle treatments, the multiconfigurational quantum chemistry methods, traditionally reserved for atoms/molecules, accurately describe the many-body characteristics of the electronic states of these defect centers and correctly predict properties that single-particle treatments fail to obtain. We choose the negatively charged nitrogen-vacancy (NV^-) center in diamond as the prototype defect to study with these techniques due to its importance for quantum information applications and because its properties are well-known, which makes it an ideal benchmark system. By properly accounting for electron correlations and including spin-orbit coupling and dipolar spin-spin coupling in the quantum chemistry calculations, for the NV^- center in diamond clusters, we are able to: (i) show the correct splitting of the ground (first-excited) spin-triplet state into two levels (four levels), (ii) calculate zero-field splitting values of the ground and excited spin-triplet states, in good agreement with experiment, (iii) determine many-body configurations of the spin-singlet states, and (iv) calculate the energy differences between the ground and excited spin-triplet and spin-singlet states, as well as their ordering, which are also found to be in good agreement with recent experimental data. The numerical procedure we have developed is general and it can screen other color centers whose properties are not well known but promising for applications.

I. INTRODUCTION

Defects in solid-state systems are naturally formed and can be implanted in a controllable fashion. Individual defects deeply embedded in wide band-gap semiconductors are known to have distinct localized electronic states within the band gap and so they behave similar to atoms or molecules. The prototype of such deep defects is the negatively charged nitrogen-vacancy (NV^-) center defect in diamond which has been extensively used for sensing^{1,2}, for the demonstration of loophole-free Bell inequalities³, and for a proof-of-principle of quantum error correction^{4,5}, to name a few among many important experiments and quantum information science applications. Its tremendous success was culminated in recent experimental realization of quantum entanglement between the spins of the NV^- centers over a kilometer range³. Single spins of the NV^- center defects were shown to be optically initialized and read out with long spin-lattice relaxation and spin coherence times at room temperature⁶⁻¹³, and the electronic spin can be coherently controlled both optically¹⁴ and via microwave fields¹⁵. This prototype defect inspired exploration of other defects, hopefully even more suitable for quantum information science applications, in diamond and other wide band-gap semiconductors such as the silicon vacancies and NV center in silicon carbide¹⁶⁻²⁰, the silicon vacancy center in diamond²¹⁻²⁵, and rare-earth defects in silicon²⁶ or yttrium orthosilicate²⁷.

Electronic and magnetic properties of deep defects have been studied using either various levels of *ab ini-*

tio theory or phenomenological molecular models based on group theory. In the quest of unexplored, improved defects, *ab-initio* theory rather than the molecular model approach can play an essential role in screening candidate defects for quantum information science applications before experimental data are available, because the latter approach requires parameter values such as Coulomb interactions and dipolar spin-spin coupling (SSC) and spin-orbit coupling (SOC) strengths. To that end, the techniques need to be reliable and predict defect properties as accurately as possible. Although single-particle *ab-initio* techniques are extensively used, they have serious limitations for strongly correlated systems, especially for excited states. For example, density-functional theory (DFT) (as well as the molecular model approach) could not correctly predict the ordering of the spin-singlet states of the NV^- center defect in diamond²⁸⁻³¹, which led to a long-standing debate and conflicting results in the community³⁰⁻³⁴. Recent experimental results resolved this conflict³⁵⁻³⁷. Furthermore, DFT could not correctly predict either the ordering or the energy difference between the excited spin-triplet and spin-singlet states of the NV^- center defect^{28,38,39}. The aforementioned incorrect predictions of DFT highly influence our understanding of optical transitions between the triplet and singlet states referred to as intersystem crossings^{6,30,33,34}, which are key mechanisms to initialize and readout the spin-polarized states for quantum technology applications.

In order to remedy this limitation, quantum chemistry calculations^{38,40,41} were performed for the NV^- center

defect in diamond clusters, but the electronic structure of the defect states is not all consistent with experimental data^{35,36,42}. For example, the ordering of the excited triplet and singlet states and the energy differences between the singlet states (or the excited triplet and singlet states) does not agree with experiment. As a middle ground, beyond-DFT *ab-initio* results were combined with model Hamiltonians within many-body (perturbation) theory^{19,25,43,44}, finding agreement with experimental data^{35-37,42}. However, this method requires fitting of the *ab-initio* results to the model Hamiltonian parameters. More importantly, within this method, accounting for the effects of SOC and SSC is not straightforward. So far, zero-field splitting values induced by SOC and/or SSC have not been studied within many-body *ab-initio* methods.

In this work, we investigate the electronic structure and magnetic properties of an NV⁻ center in diamond by systematically applying multiconfigurational quantum chemistry methods (beyond DFT) to hydrogen-passivated diamond clusters containing the defect. The critical ingredient for success in quantum chemistry calculations is to include several defect-localized unoccupied states beyond dangling bond states, which differentiates our case from the previous quantum chemistry calculations^{38,40,41}. By considering full electron correlation among these extra defect states and the dangling bond states, we determine excitation energies between the ground state and the excited spin-triplet and spin-singlet states as well as the character of the states. Furthermore, using the quantum chemistry methods, we examine effects of SOC and SSC on the spin-triplet states and identify characteristics of the split levels as well as the zero-field splitting values. To the best of our knowledge, this work is the first quantum chemistry calculation of the zero-field splitting by SOC and SSC for an NV⁻ center in diamond. Our calculated results of the electronic structure and zero-field splitting are compared to recent experimental data with which we find agreement ranging from good to excellent.

This paper is structured as follows. In Section II we provide a brief overview of the NV⁻ center in diamond. In Section III we describe the structures of the clusters that are considered. In Section IV we discuss our procedure of applying the quantum chemistry methods to the diamond clusters, while the technical detail with a flowchart is provided in the Appendix. In Section V we present our results of the energy separations and characteristics of the triplet and singlet states as well as the zero-field splitting in comparison to other theoretical studies and experimental data. In Section VI we provide our conclusion and outlook.

II. OVERVIEW OF NV⁻ CENTER DEFECT

The deep NV⁻ center defect in diamond consists of a nitrogen atom substituting for carbon and a vacancy at

its neighboring carbon site, as shown in Fig. 1(a). The axis connecting between the vacancy and nitrogen sites is chosen to be the z axis. The defect has a C_{3v} point-group symmetry comprising two threefold rotational symmetries (C_3) about the z axis and three vertical mirror planes σ_i ($i = 1, 2, 3$) each passing through the nitrogen and nearest carbon atoms in the xy -plane (Fig. 1).

For an NV⁻ center in diamond, experimental zero-phonon absorption spectra showed that the ground state is a spin-triplet 3A_2 state with an excitation energy of 1.945 eV to the first-excited spin-triplet 3E ⁴² and that the excitation energy between the lowest and first-excited spin-singlet states ($^1E-^1A_1$) is 1.190 eV³¹. Recent experimental data^{35,36} showed that the singlet 1A_1 state has a higher energy than the singlet 1E state. So far, there have been no direct measurements on the excitation energy of the spin-singlet 1E state relative to the ground 3A_2 state. This excitation energy, however, can be deduced from the experimental energy difference between the 3E and 1A_1 states (which is in the range of 0.321 to 0.414 eV^{36,37}) as well as from the $^1A_1-^1E$ energy difference.

III. CLUSTER STRUCTURES

To study the NV⁻ center in diamond, we consider two vacancy-centered clusters with hydrogen passivation, $C_{33}H_{36}N^-$ (70-atom cluster) and $C_{85}H_{76}N^-$ (162-atom cluster), which are created such that they have the correct C_{3v} symmetry. The geometries of the clusters are constructed from the DFT-optimized, C_{3v} -symmetric structure of a 215-atom cubic supercell with an NV⁻ center. The DFT calculation of the relaxation is performed for the cubic supercell with $4 \times 4 \times 4$ k -points within the Perdew-Burke-Ernzerhof (PBE)⁴⁵ generalized gradient approximation using Quantum Espresso⁴⁶. Ultrasoft pseudopotentials with scalar relativistic terms and non-local core corrections are used until the maximum residual force is less than 0.005 eV/Å. Figure 1 shows side and top views of the 70-atom cluster and a top view of the 162-atom cluster where the z axis is along the body-diagonal [111] direction in the cubic supercell. After the geometry optimization, the C_{3v} point-group symmetry is retained at the NV⁻ center in the supercell. For the DFT-optimized supercell, the bond length between the nitrogen atom and the carbon atoms nearest to the vacancy is 2.734 Å, and the bond lengths between two nearest neighboring carbon atoms closest to the vacancy is 2.676 Å. These bond lengths agree well with the corresponding bond lengths reported from other DFT calculations⁴⁷. The shortest distance between the vacancy and carbon (nitrogen) is 1.647 (1.690) Å. For the clusters, the bond length between hydrogen and carbon is set to a standard value, 1.09 Å, and no further relaxation is carried out.

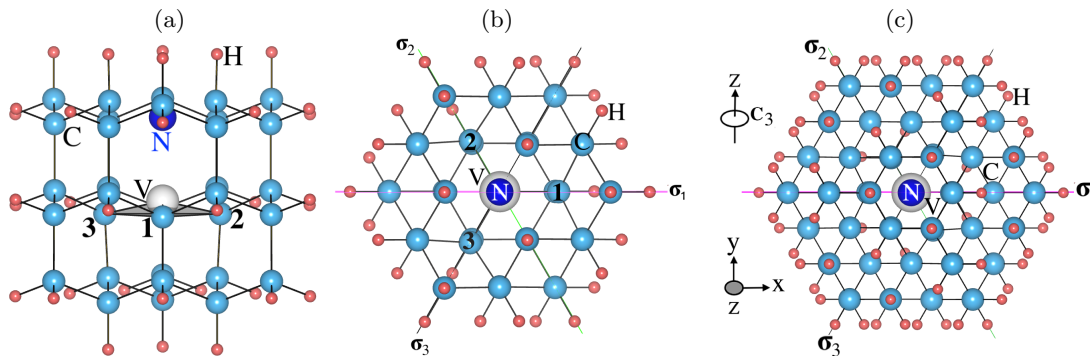


FIG. 1. (a) Side view and (b) top view of the NV^- center defect in a 70-atom diamond cluster with C_{3v} symmetry. (c) Top view of the NV^- center defect in a 162-atom cluster with C_{3v} symmetry. The color scheme is as follows: carbon (cyan), nitrogen (blue), vacancy (grey), hydrogen (pink). Carbon, nitrogen, vacancy, and hydrogen are denoted by C, N, V, and H, respectively. The rotation axis of the three-fold symmetry (C_3) and the coordinate axes are shown. Here σ_1 , σ_2 , and σ_3 indicate vertical mirror planes passing through the carbons nearest to the vacancy with broken dangling bonds (labeled by 1, 2, and 3), the vacancy, and the z axis.

IV. QUANTUM CHEMISTRY METHODS

The quantum chemistry calculations are carried out in two steps: (i) complete active space self-consistent field (CASSCF) calculations with state average⁴⁸; (ii) inclusion of SOC and SSC. We use both the `OpenMolcas`⁴⁹ code and the `ORCA`^{50,51} code. The scalar relativistic effects are included based on the Douglas-Kroll-Hess Hamiltonian using relativistically contracted all-electron correlation-consistent polarized double-zeta basis sets, cc-pVDZ-DK^{52,53}, for all atoms in the clusters. A schematic flow chart of our computational procedure is shown in Fig. 2(c).

A. CASSCF calculations

In the CASSCF formalism⁴⁸, a many-body wave function is described as a linear combination of multiple Slater's determinants, each of which is made of single-electron molecular orbitals. The coefficients of the Slater's determinants are referred to as configuration interaction (CI) expansion coefficients. A CASSCF wave function is partitioned into parts from inactive orbitals with double occupancy, virtual orbitals with zero occupancy, and active orbitals with occupancy between zero and two (i.e., 0, 1, or 2). In a CASSCF calculation, for a given spin multiplicity, any possible electron configurations or correlation within the active orbital space are included, while keeping the occupancies of the inactive and virtual orbitals fixed. However, electron excitation or correlations outside the active space are not included. Both the CI coefficients and the molecular orbitals are optimized through self-consistent calculations. Therefore, the choice of the active orbitals is critical for accurate CASSCF calculations. It was shown that the accuracy of CASSCF calculations is greatly improved by including extra molecular orbitals beyond frontier orbitals in the

active space⁴⁸. CASSCF wave functions are described in terms of spin-free basis states that correspond to all possible configurations generating the maximum M_z values, where M_z is an eigenvalue of the S_z operator (i.e., the z component of the total spin S). The state-average is a technique to facilitate convergence of the excited-state CASSCF wave functions⁴⁸.

In order to determine the number and character of orbitals to be included in the active space, we start with a qualitative analysis of the electronic structure of an NV^- center from a single-electron point of view. The NV^- center in diamond has four broken dangling bonds, as shown in Fig. 1(a): three dangling bonds of the nearest neighboring carbon atoms to the vacancy (d_1 , d_2 , and d_3), and the dangling bond of the nitrogen atom to the vacancy (d_N). They form four single-electron molecular orbitals such as $a_1^C = (d_1 + d_2 + d_3)/3$, $a_1^N = d_N$, $e_x = (2d_1 - d_2 - d_3)/\sqrt{2}$, and $e_y = (d_2 - d_3)/\sqrt{2}$ ^{29,54,55}. The first two orbitals transform as a function of the A_1 irreducible representation (IRRep), and the other two orbitals transform as functions of the E IRRep under the C_{3v} point group. It is known that the a_1^N orbital is deeply buried under the valence band of the diamond lattice, whereas the other three orbitals are within the band gap^{28,29,54,55}. These three states are also referred to as in-gap defect states¹⁹. Now let us count the total number of electrons in the system. A carbon vacancy within diamond leaves four electrons in four dangling bonds. One of these carbon-atoms is substituted with a nitrogen-atom that has an extra electron (as compared to a carbon atom). The defect further acquires an additional electron and becomes negatively charged, resulting in a total number of six electrons that fill the defect states in accordance with the Hund's rules. In the spin-triplet ground-state, the *nominal* occupancy is as follows: the defect state, a_1^N , which lies in the valence band, is doubly occupied, while the remainder of the four electrons are distributed amongst the in-gap states, with a_1^C being

doubly occupied, and the degenerate orbitals, $(e_x e_y)$, being singly occupied.

Inspired by the single-electron picture, we initially perform CASSCF calculations using the active space consisting of six electrons and the four dangling bond orbitals $(a_1^N, a_1^C, e_x, \text{ and } e_y)$ for the 70-atom and 162-atom diamond clusters with C_{3v} symmetry, shown in Fig. 2(a) and (b). These calculations are referred to as CASSCF(6,4) following the number of electrons and orbitals used in the active space. The excitation energies obtained via CASSCF(6,4) calculations are highly overestimated as compared to experiment and the excited-state wave functions are found to be inconsistent with physical and chemical intuitions. As a result, we expand the active space by including extra unoccupied defect-localized states. The most common practice is to identify these extra states in the virtual space of the converged CASSCF(6,4) result. However, no such defect orbitals are found in the virtual space. Therefore, we introduce a series of CASSCF calculations discussed in the Appendix (Fig. 6) in order to identify and include extra defect orbitals in the active space. With this systematic CASSCF procedure, we find two unoccupied defect orbitals with E IRRep. In order to distinguish them from the dangling bond orbitals, e_x and e_y , they are, henceforth, referred to as e'_x and e'_y (Fig. 2(a) and (b)). The e'_x and e'_y orbitals are expected to lie in the conduction band region (i.e., defect orbitals are resonant with the conduction band). With these two extra unoccupied orbitals, as well as, the four dangling bond orbitals, we form an active space consisting of six electrons and six orbitals, and carry out CASSCF(6,6) calculations for both the total spin $S = 1$ and $S = 0$. Furthermore, in order to achieve high accuracy and exact numerical degeneracy (up to ~ 10 neV) in states with E symmetry, we carefully maintain the IRRep symmetry of all of the molecular orbitals and remove the surface-dominant orbitals in the self-consistent calculations.

B. Spin-orbit coupling and spin-spin coupling

For the ground 3A_2 state, the first-order SOC effect on the zero-field splitting vanishes and higher-order terms are negligibly small due to weak SOC. However, for the first-excited 3E state, the first-order SOC effect becomes important within the subspace of degenerate states and the SOC-induced splitting turns out to be non-negligible. Therefore, for the most accurate calculation of SOC-induced splitting, we need to describe degenerate states the most accurately. In order to achieve this, state average is carried out only over the first-excited triplet pair (3E) of the CASSCF(6,6) wave functions. Then SOC is included in the converged CASSCF(6,6) spin-triplet wave functions within the atomic mean-field approximation⁵⁷, using the restricted active space state interaction (RASSI) method⁵⁸ implemented in `OpenMolcas`. For the CASSCF(6,6) energy eigenvalues and the SOC-induced

zero-field splitting, `OpenMolcas` is used because it provides more accurate results due to purely symmetric orbitals and removal of surface-dominated orbitals (see the Appendix).

The zero-field splitting by the SSC is expected for all spin-triplet states. This feature is computed for the CASSCF(6,6) wave functions using `ORCA` because it is not available in `OpenMolcas`. The SSC is calculated as the two-electron direct SSC over the CASSCF(6,6) wave functions using first-order perturbation theory⁵⁹, as implemented in `ORCA`. The CASSCF(6,6) wave functions using `ORCA` are obtained by following the CASSCF procedure sketched in the Appendix without orbital symmetrization, `SUPERSYMMETRY` keyword, and removal of surface orbitals, because they are not available in `ORCA`. We confirm that the zero-field splitting induced by SSC is not sensitive to technical details of the calculations (i.e., the cluster size, the size of the active space and the number of roots included in the state average).

V. RESULTS AND DISCUSSION

A. Excitation energies

Figure 3 shows schematic level diagrams of our calculated spin-triplet and spin-singlet states for the two cluster sizes using `OpenMolcas` (quantum-chemistry methods, CASSCF(6,6)). Note that we use the ground-state geometry without phonon modes and that we do not consider structural relaxation of the electronic excited states. An experimental absorption spectrum of an NV^- center in diamond consists of a sharp zero-phonon line with a broad spectrum of phonon side bands with several peaks^{35,42}. With significant electron-phonon coupling, a zero-phonon absorption energy can noticeably differ from a vertical excitation energy. The latter energy is always higher than the former energy. The latter energy is commonly experimentally obtained from the maximum-intensity peak of the broad phonon side-band spectrum. The broadness of the phonon side bands provides some uncertainty in the maximum-intensity peak energy, which renders uncertainty in the experimental vertical excitation energy. For comparison to experiment, we provide both experimental zero-phonon absorption energies and experimental vertical excitation energies in Fig. 3.

Our calculations show that the first-excited spin-triplet 3E state is separated from the ground state (3A_2) by 1.93 and 2.14 eV for the 70-atom and 162-atom clusters, respectively. This energy separation does not depend much on the cluster size and it is close to the experimental energies of zero-phonon absorption, 1.945 eV, and of vertical excitation, 2.18 eV⁴². We find that the lowest-energy singlet state has character of 1E and that the first-excited singlet 1A_1 state is located at 1.07 eV and 1.35 eV above the 1E state for the 70-atom and 162-atom clusters, respectively. The ordering and the character of the singlet

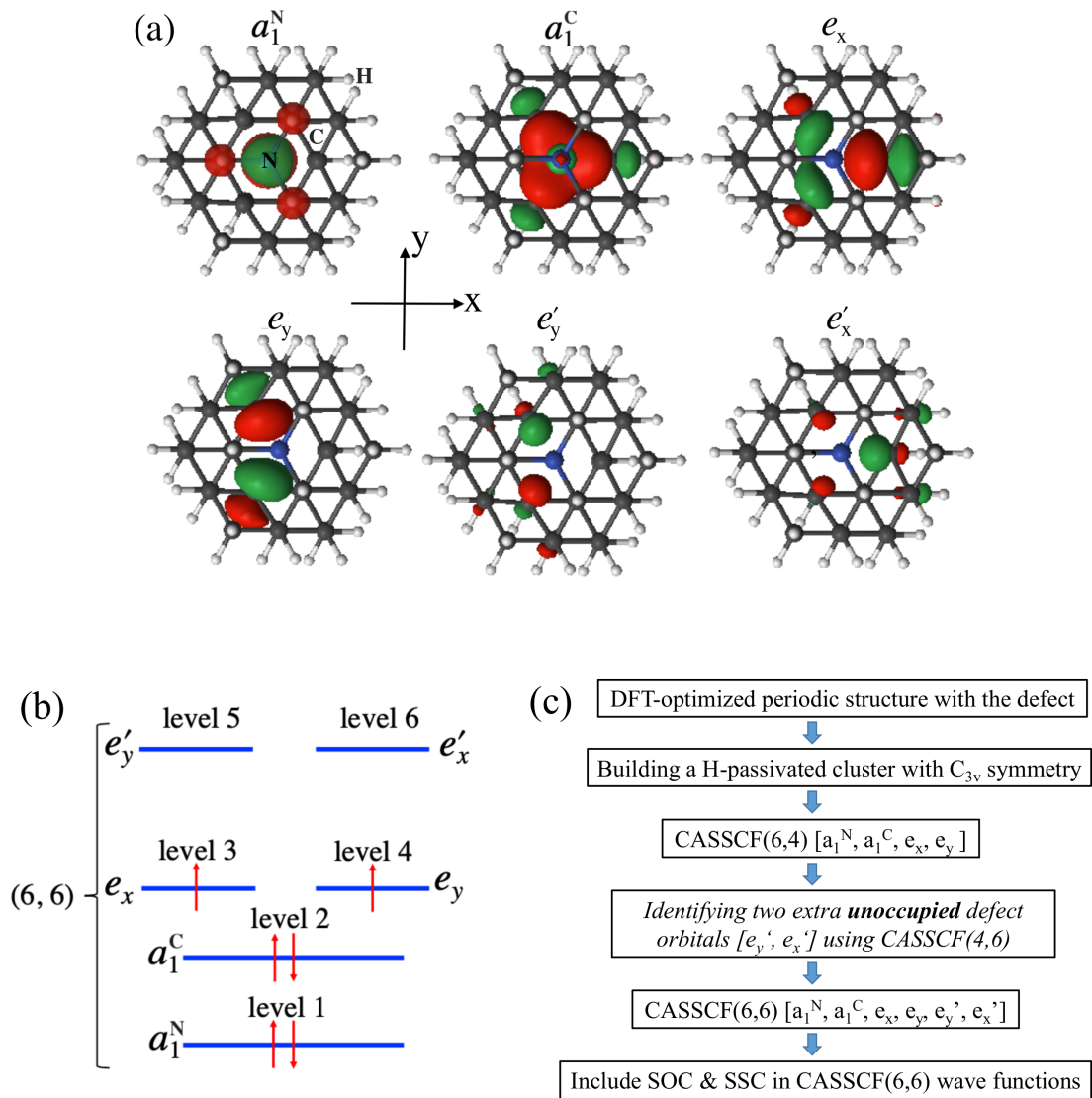


FIG. 2. (a) Top view of six defect orbitals (belonging to two A_1 and four E IRRep) in the active space with iso-surface value of 0.06 for the CASSCF(6,6) calculation of the 70-atom cluster. The similar six active orbitals are identified for the 162-atom cluster. The LUSCUS program⁵⁶ is used for visualization. (b) Nominal distribution of six electrons over the six active orbitals in the ground spin-triplet (3A_2) state. The actual occupation numbers of the a_1^N , a_1^C , e_x , e_y , e'_x , e'_y , are found to be 1.9986, 1.3753, 0.9883, 0.9883, 0.3248, and 0.3248, respectively, from the CASSCF(6,6) calculation. (c) Schematic flowchart of our computational procedure in which the italicized step is discussed in detail in the Appendix.

states agree with experiment, considering the experimental energies of zero-phonon absorption, 1.190 eV³¹, and of vertical excitation, 1.26 eV³⁵. Our results also reveal the energy differences between the triplet and singlet states. The 1E state lies at 0.34 eV and 0.25 eV above the 3A_2 state for the 70-atom and 162-atom clusters, respectively. As a result, the energy gap between the 3E and 1A_1 states becomes 0.52 and 0.54 eV for the 70-atom and 162-atom clusters, respectively. Although the energy gap between the 3A_2 state and the 1E state has not been directly experimentally measured, the separation between the 3E state and the 1A_1 state was measured to be 0.321-0.414 eV^{36,37}, which is in good

agreement with our results. The second-excited (third-excited) triplet state has characteristics of 3A_1 (3E). The second-excited singlet 1A_2 state appears even above the third-excited triplet 3E state. There are no experimental reports on the higher-energy levels or separations.

Our calculated results show that for the four lowest states (3A_2 , 3E , 1E , and 1A_1) the energy eigenvalues do not depend much on the cluster size. However, we find that the cluster-size dependence becomes more apparent for higher-energy states, especially for the second- and third-excited triplet states (3A_1 and 3E). Depending on the cluster size, the energy separations change but the ordering of the states does not change. A similar trend of

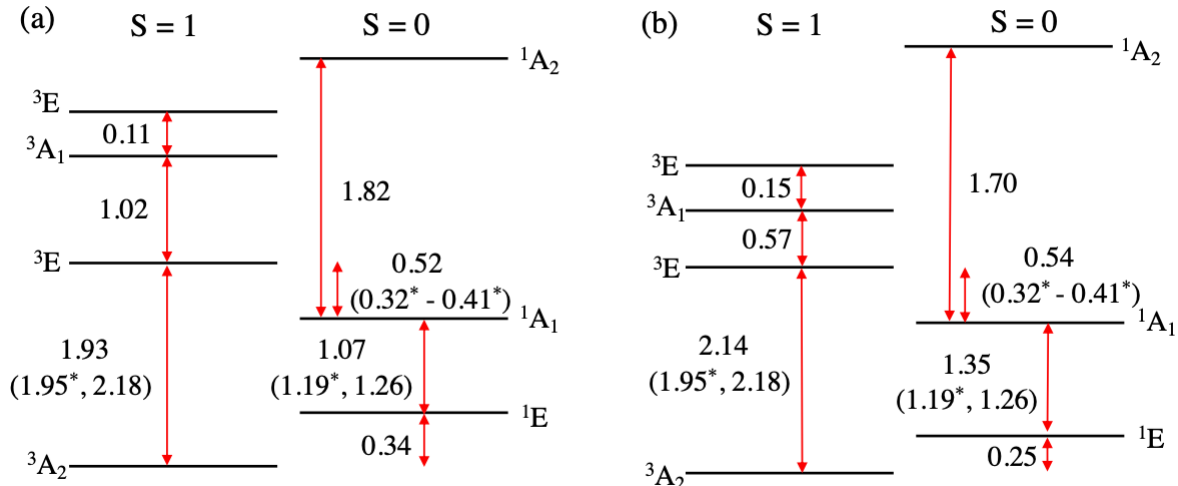


FIG. 3. Schematic level diagrams of the spin-triplet and spin-singlet states for (a) the 70-atom and (b) the 162-atom diamond clusters obtained using the quantum-chemistry method without SOC or SSC. Here full electron correlation within the six molecular orbitals [Fig. 2(a) and (b)] are considered. The experimental values^{31,35–37,42} are shown inside parentheses. The experimental zero-phonon absorption energies are marked with *. All energy values are given in units of eV.

the cluster-size dependence was reported in the complete-active space approach, using DFT Kohn-Sham orbitals and density-matrix renormalization group⁶¹. This trend can be understood by the fact that higher-energy levels have stronger electron correlations which requires inclusion of more empty orbitals in the active space. Since experimental data are available for mainly up to the first-excited triplet 3E state, we do not further study an effect of cluster size on the electronic structure.

B. Comparison to other *ab-initio* studies

Let us now compare our calculated energies of the spin-triplet and spin-singlet states (3A_2 , 3E , 1E , and 1A_1) to the previous *ab-initio* theoretical studies. See Table I and Fig. 4. In our analysis, we focus on the four lowest states because only the level separations among them were experimentally measured and because higher-energy states are more sensitive to the cluster size and the size of the active space. (For example, the higher-energy ${}^1E'$ state that many-body theory studies predicted^{19,43,44} has not been observed³⁵.) We first discuss comparison to other DFT calculations and then to other quantum-chemistry studies as well as many-body theory studies, separately.

Earlier DFT studies of an NV^- center in diamond clusters and periodic supercells^{28,38,39,41,62,63} showed that the calculated excitation energy of the 3E state more or less agrees with our result and experiment except for Ref.³⁸. However, DFT-calculated energies of the singlet states are scattered in a wide range and the ordering of the triplet and singlet states is inconsistent with recent experiment. This trend is understandable considering that

DFT poorly describes the singlet states due to the well-known spin contamination effect.

In the previous quantum-chemistry studies of an NV^- center in diamond clusters^{38,40,41}, either the excitation energies are significantly different from experiment, or the ordering of the singlet and triplet states is reversed. More specifically, CASSCF(6,8) calculations discussed in Ref.⁴¹ showed that the excitation energy of the 3E state is 0.5-0.6 eV (0.3-0.4 eV) higher than our result (experiment). The singlet states were not investigated in that work. In the CASSCF(8,11) calculations presented in Ref.⁴⁰, the excitation energy of the 3E state is about 1.0 eV lower than our result or experiment, and the singlet 1A_1 state is slightly above the triplet 3E state, which does not agree with our result or recent experiment. Their multireference configuration interaction (MRCI) calculations⁴⁰ somewhat increase the energies of the triplet and singlet states with the correct ordering of the excited triplet and singlet states. However, the energy of the 3E state remains lower than our value by about 0.6 eV. Monte Carlo configuration interaction (MCCI) studies³⁸ showed the energy of the 3E state in agreement with our result and experiment. However, the ordering of the 3E and 1A_1 states is reversed. See Table I and Fig. 4. The discrepancies between our results and all of the earlier quantum-chemistry calculations arise from the choice of orbitals in the active space. One of the most common ways to choose active orbitals is to use single-electron molecular orbitals in the vicinity of the band gap such as orbitals near the highest occupied molecular orbitals (HOMO) and lowest unoccupied molecular orbitals (LUMO). For a hydrogen-passivated diamond cluster with an NV^- center, either this common prac-

TABLE I. Our calculated excitation energies with respect to the ground state (3A_2) in units of eV for the two cluster sizes using the quantum chemistry method (without SOC or SSC), in comparison to previous theoretical studies and experimental data. For our calculations, neither the relaxation energy of the excited states nor vibration energies are included. In other words, we use the same geometry for the ground state and all excited triplet and singlet states. Zero-phonon absorption energies are marked with *. The unmarked experimental value correspond to the vertical excitation energy, i.e. the maximum-intensity peak energy of the phonon side band spectra⁴². The experimental energy of the 1E state relative to the ground-state energy is converted from the following two measurements: (a) the zero-phonon absorption energy between the 1E and 1A_1 states which is 1.190 eV³¹; (b) the energy difference between the 1A_1 and 3E states which is 0.321-0.414 eV^{36,37}.

Reference \ Electronic State	3E	3A_1	3E	1E	1A_1	1A_2
Experiment ^{31,35-37,42}	1.945* ⁴² ~2.18 ⁴²			0.34*-0.43* 36,37	1.51*-1.60* 31	
C ₃₃ H ₃₆ N ⁻ CASSCF(6,6) (This work)	1.93	2.95	3.06	0.34	1.41	3.23
C ₈₅ H ₇₆ N ⁻ CASSCF(6,6) (This work)	2.14	2.71	2.86	0.25	1.60	3.30
C ₃₃ H ₃₆ N ⁻ CASSCF(6,8) ⁴¹	2.48					
C ₄₉ H ₅₂ N ⁻ CASSCF(6,8) ⁴¹	2.57					
C ₁₉ H ₂₈ N ⁻ CASSCF(8,11) ⁴⁰	0.98		1.22	0.44	1.00	1.13(1E)
C ₁₉ H ₂₈ N ⁻ MRCI(8,10) ⁴⁰	1.36		1.61	0.50	1.23	1.37(1E)
C ₄₂ H ₄₂ N ⁻ MCCI ³⁸	1.96, 1.93			0.63, 0.64	2.06	
<i>GW</i> +BSE ⁴³	2.32			0.40	0.99	2.25(${}^1E'$)
<i>GW</i> fit to model ⁴⁴	2.0*			~0.5	~1.5	~3.0(${}^1E'$)
	2.1					
CI-CRPA ¹⁹	1.75*			0.49	1.41	3.09(${}^1E'$)
(512-atom supercell)	2.02					
Beyond-RPA ²⁵ with quantum embedding theory	2.00			0.56	1.76	
C ₃₃ H ₃₆ N ⁻ DFT ⁶⁰	1.77*			0.44	1.67	
DFT (512-atom supercell) ²⁸	1.71*			0.9	0.0, 2.2	
C ₄₂ H ₄₂ N ⁻ DFT ³⁸	1.91					
	1.27			0.42	2.10	
					1.26(${}^1A'$)	
C ₂₈₄ H ₁₄₄ N ⁻ DFT ³⁸	1.90			0.48	2.03	
					1.26(${}^1A'$)	

tice within CASSCF or MRCI, or an automatic choice of the active space in MCCI may result in non-physical surface-dominated orbitals in the CI basis set. As shown in Fig. 2(a), in our case, all six orbitals in the active are localized near the vacancy defect.

An earlier many-body perturbation study⁴³ based on the *GW* approximation with Bethe-Salpeter equation (BSE) provided the singlet-singlet (1A_1 - 1E) energy difference about 0.6 eV lower than our result and recent experiment^{35,36}, although the energy of the 1E state relative to the ground state, as well as the ordering of the two singlet states are in agreement with the recent experimental data. On the other hand, recent many-body studies^{19,25,44} showed more promising results by using effective many-body model Hamiltonians with parameters obtained from (or fitted to) *ab-initio* calculations in order to properly include many-body character in the wave functions. For example, additional unoccupied defect states (resonant to the conduction band) and doubly occupied defect states (in the valence band) were included in the configuration interaction constrained random phase approximation (CI-CRPA) method¹⁹. This is analogous to our inclusion of unoccupied level 5 and 6 and doubly oc-

cupied level 1 [Fig. 2(b)] in the active space for proper treatment of electron correlation. Their results are closest to our result among the previous studies that we have discussed (see Fig. 4 and Table I). Yet, there are some differences. In the fitting of *GW*-calculated bands to model Hamiltonian⁴⁴ (in the CI-CRPA method¹⁹), the singlet-singlet energy difference is about 0.2-0.3 eV (0.3-0.4 eV) lower than our result and experiment. In the beyond-RPA implemented in the quantum embedding theory²⁵, the energy difference between the 3E and 1A_1 states is somewhat smaller than our result and experiment. This discrepancy may arise from missing orbital configurations in the 1E and 1A_1 states in Refs.^{19,25,44} that are discussed in Sec.V C. Here we stress that it does not seem to be straightforward to include effects of SOC and SSC within the formalisms used in Refs.^{19,25,44} in contrast to the quantum chemistry methods where such effects can be added to the many-body wave functions without an introduction of new fitting parameters (see Sec.V D).

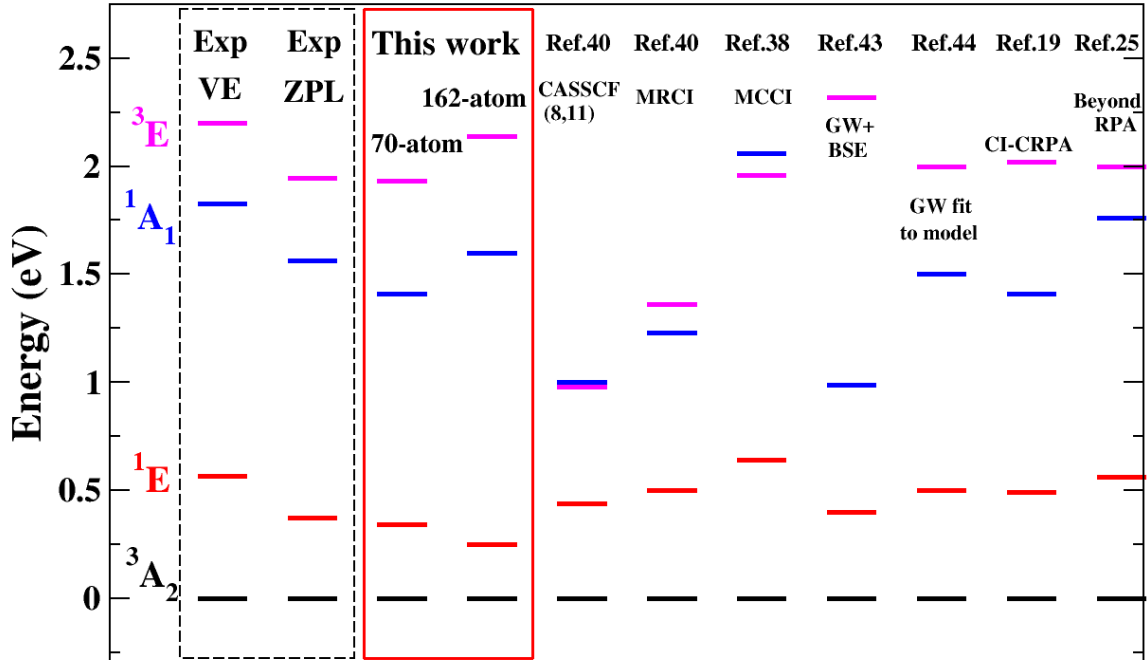


FIG. 4. Comparison of our calculated spin-triplet and spin-singlet energies to the previous many-body theoretical studies^{19,25,38,40,43,44} as well as the experimental zero-phonon lines (ZPL) and vertical excitations (VE)^{31,35–37,42}. The experimental VE are energies of the maximum-intensity peak of the broad phonon side-band absorption spectra. The experimental ZPL and VE energies of the 1E and 1A_1 states (relative to the ground state) are taken from the mid point of the experimental range³⁶ of the separation between the 3E and 1A_1 states, while keeping the $^1A_1 - ^1E$ energy difference fixed as the experimental value of 1.190 eV³¹.

C. Characteristics of energy eigenstates

We now discuss characteristics of our calculated triplet and singlet energy eigenstates (Table II). Here we use configuration basis states which are all possible states generating the maximum M_z value from the six active orbitals for a given total spin S , where M_z is an eigenvalue of the S_z operator. The total wave functions in terms of true S_z eigenstates are obtained when SOC is applied to the many-body (CASSCF) wave functions within the RASSI method⁵⁸ using the Wigner-Eckart theorem. The SOC effect is discussed later in Sec. VD.

For the ground and first-excited triplet states, the configurations of our calculated eigenstates are similar to those identified from the phenomenological molecular models based on group theory^{54,55,64}, as long as we focus on the configurations with weights greater than 10%. However, for the *singlet* states, we find that the following additional configurations significantly contribute: $\uparrow\downarrow\uparrow\downarrow\uparrow\downarrow\uparrow\downarrow$ and $\uparrow\downarrow\uparrow\uparrow\downarrow\downarrow\uparrow\downarrow$ with 12% each for the 1E state and $\uparrow\downarrow\uparrow\downarrow\uparrow\downarrow\uparrow\downarrow$ with 20% for the 1A_1 state. Refer to Table II for the notations. The former states indicate single-excitations from the doubly occupied a_1^C level, while the latter state indicates a double-excitation from the a_1^C level. These configurations have not been considered before in the literature. Their inclusion in our

work may have given rise to the discrepancy between our result and those obtained in Refs.^{19,25,44} and it may also affect the intersystem crossing.

Furthermore, above the first-excited triplet 3E state and the first-excited 1A_1 state, we find the triplet 3A_1 and 3E states and the singlet 1A_2 state. Due to the lack of experimental data beyond the four lowest states, we only briefly mention these higher-energy states. Our higher-energy states differ from those in the literature^{19,40,43,44,54,55}. As shown in Table II, the main contributions to these states originate from single excitations from the a_1^C , e_x , or e_y orbital to beyond the dangling bond orbitals (e'_x and e'_y) (Fig. 2(b)). On the other hand, the previous many-body and molecular-model studies^{43,44,54,55} were mostly obtained considering only three or four dangling bond orbitals (a_1^N , a_1^C , e_x , and e_y). As discussed earlier, the higher-energy states are more sensitive to the size of active space and cluster size than the four lowest states due to stronger electron correlation. Note that the $^1E'$ state predicted in the literature has not been experimentally observed³⁵.

TABLE II. Characteristics of the calculated energy eigenstates for the 70-atom cluster using the configuration (spin-free) basis states. Here the configuration basis states are all possible states generating the maximum M_z value from the six active orbitals (Fig. 2) for a given total spin S , where M_z is an eigenvalue of S_z . Each box represents an orbital. Up and down arrows denote spin-up and spin-down electrons. Each configuration represents a Slater's determinant of the orbitals with $2S + 1$ degeneracy. Percentages denote orbital configuration weights. Only configurations with weights greater than 5% or above are listed. Weights greater than 10% are denoted as boldface.

State	Configuration (weight)	a_1^N	a_1^C	e_x	e_y	e'_y	e'_x
${}^3A_2(\Psi_{1,T})$	$\uparrow\downarrow\uparrow\downarrow\uparrow\uparrow\uparrow$ (94%)						
${}^3E(\Psi_{2,T})$	$\uparrow\downarrow\uparrow\uparrow\uparrow\uparrow\uparrow$ (38%), $\uparrow\downarrow\uparrow\uparrow\uparrow\uparrow\downarrow$ (31%), $\uparrow\downarrow\uparrow\uparrow\uparrow\downarrow\uparrow$ (7%), $\uparrow\downarrow\uparrow\uparrow\uparrow\downarrow\downarrow$ (5%)						
$(\Psi_{3,T})$	$\uparrow\downarrow\uparrow\uparrow\uparrow\downarrow\uparrow$ (38%), $\uparrow\downarrow\uparrow\uparrow\downarrow\uparrow\uparrow$ (30%), $\uparrow\downarrow\uparrow\uparrow\uparrow\downarrow\downarrow$ (7%), $\uparrow\downarrow\uparrow\uparrow\uparrow\downarrow\uparrow$ (5%)						
${}^3A_1(\Psi_{4,T})$	$\uparrow\downarrow\uparrow\downarrow\uparrow\uparrow\uparrow$ (29%), $\uparrow\downarrow\uparrow\downarrow\uparrow\uparrow\uparrow$ (29%), $\uparrow\downarrow\uparrow\uparrow\downarrow\uparrow\uparrow$ (9%), $\uparrow\downarrow\uparrow\uparrow\downarrow\uparrow\downarrow$ (6%), $\uparrow\downarrow\uparrow\uparrow\uparrow\downarrow\uparrow$ (6%), $\uparrow\downarrow\uparrow\uparrow\downarrow\uparrow\downarrow$ (6%), $\uparrow\downarrow\uparrow\uparrow\uparrow\uparrow\uparrow$ (6%)						
${}^3E(\Psi_{5,T})$	$\uparrow\downarrow\uparrow\downarrow\uparrow\uparrow\uparrow$ (22%), $\uparrow\downarrow\uparrow\downarrow\uparrow\uparrow\uparrow$ (22%), $\uparrow\downarrow\uparrow\uparrow\uparrow\downarrow\uparrow$ (14%), $\uparrow\downarrow\uparrow\uparrow\downarrow\uparrow\uparrow$ (6%), $\uparrow\downarrow\uparrow\uparrow\uparrow\downarrow\downarrow$ (5%)						
$(\Psi_{6,T})$	$\uparrow\downarrow\uparrow\downarrow\uparrow\uparrow\uparrow$ (22%), $\uparrow\downarrow\uparrow\downarrow\uparrow\uparrow\uparrow$ (22%), $\uparrow\downarrow\uparrow\uparrow\uparrow\downarrow\uparrow$ (14%), $\uparrow\downarrow\uparrow\uparrow\downarrow\uparrow\uparrow$ (6%), $\uparrow\downarrow\uparrow\uparrow\uparrow\downarrow\downarrow$ (5%)						
${}^1E(\Psi_{1,S})$	$\uparrow\downarrow\uparrow\downarrow\uparrow\downarrow\uparrow$ (34%), $\uparrow\downarrow\uparrow\downarrow\uparrow\downarrow\uparrow$ (34%), $\uparrow\downarrow\uparrow\downarrow\downarrow\uparrow\downarrow$ (12%), $\uparrow\downarrow\uparrow\downarrow\uparrow\downarrow\downarrow$ (7%)						
$(\Psi_{2,S})$	$\uparrow\downarrow\uparrow\downarrow\uparrow\downarrow\downarrow$ (69%), $\uparrow\downarrow\uparrow\downarrow\uparrow\downarrow\uparrow$ (12%)						
${}^1A_1(\Psi_{3,S})$	$\uparrow\downarrow\uparrow\downarrow\uparrow\downarrow\uparrow$ (29%), $\uparrow\downarrow\uparrow\downarrow\uparrow\downarrow\uparrow$ (29%), $\uparrow\downarrow\uparrow\downarrow\uparrow\downarrow\downarrow$ (20%)						
${}^1A_2(\Psi_{4,S})$	$\uparrow\downarrow\uparrow\downarrow\uparrow\downarrow\downarrow$ (32%), $\uparrow\downarrow\uparrow\downarrow\uparrow\downarrow\downarrow$ (32%), $\uparrow\downarrow\uparrow\uparrow\uparrow\downarrow\downarrow$ (6%), $\uparrow\downarrow\uparrow\downarrow\uparrow\downarrow\downarrow$ (6%)						

TABLE III. Calculated SOC- and SSC-induced level splitting of the ground state (3A_2) and the first-excited triplet (3E) state from the quantum chemistry method for the 70-atom and 162-atom clusters in comparison to experiment. The level splitting values for the 162-atom cluster are shown in the parentheses. All energies are expressed relative to the lowest SOC-included energy in each triplet state (3A_2 or 3E). One exception is the experimental zero-field splitting of the 3A_2 state marked by † in which only the difference is known. The eigenvectors including SOC, $\Psi_{1,\dots,9}$, are defined in Table IV.

State		SOC (GHz) (Theory)	SSC (GHz) (Theory)	SOC+SSC (Theory, GHz)	SOC (GHz) (Exp.) ⁶⁵	SOC+SSC (Exp., GHz) ⁶⁵
3A_2	Ψ_1	0	-1.9	-1.9	0	0 [†]
	Ψ_2, Ψ_3	0	0.8	0.8	0	2.88 [†]
3E	Ψ_4, Ψ_5	0	0.8	0.8 (0.8)	0	0.47
	Ψ_6, Ψ_7	6.5 (8.1)	-1.9	4.6 (6.2)	5.3	4.36
	Ψ_8	13.0 (16.2)	-3.1	9.9 (13.1)	10.6	9.52
	Ψ_9	13.0 (16.2)	5.3	18.3 (21.5)	10.6	12.62

D. Zero-field splitting

All of the spin-triplet states that we discussed earlier are split due to SOC and/or SSC. Note that SOC plays an important role in the zero-field splitting only for the degenerate levels in this system because of the weak SOC. Since experimental data do not exist for higher-energy states, we present calculated zero-field splitting values of the ground 3A_2 state and the first-excited triplet 3E state only. Figure 5 and Table III show our calculated level splitting by SOC alone and by SOC in combination with SSC (SOC+SSC) for the 3A_2 and 3E states,

separately, compared to experimental data⁶⁵. Table IV lists the corresponding eigenvectors $\Psi_{1,\dots,9}$ obtained from the quantum chemistry calculations including SOC and SSC. The SOC-induced level splitting is obtained for the 70-atom and 162-atom clusters, while the SSC-induced splitting is obtained for the 70-atom cluster. Regarding the SOC+SSC induced splitting for the 162-atom cluster, we use the SSC-induced splitting for the 70-atom cluster since the SSC-induced splitting does not depend much on cluster size. Let us now discuss the 3A_2 and 3E states separately.

The SOC does not split the 3A_2 state to the first order

TABLE IV. Energy eigenvalues and eigenvectors corresponding to the ground- and first-excited triplet 3A_2 and 3E states for the 70-atom and 162-atom clusters calculated using the quantum chemistry methods including SOC and SSC. The energies are relative to the lowest SOC-included energy of each triplet state (3A_2 or 3E), as listed in Table III and shown in Fig. 5. The energy values in the parentheses are for the 162-atom cluster. Here $\Psi_{1,T}$, $\Psi_{2,T}$, and $\Psi_{3,T}$ are our calculated eigenstates (without SOC and SSC) listed in Table II.

State	Energy (GHz)	Total wave function	
3A_2	Ψ_1	-1.9 (-1.9)	
	Ψ_2	0.8 (0.8)	
	Ψ_3	0.8 (0.8)	
3E	Ψ_4	0.8 (0.8)	
	Ψ_5	0.8 (0.8)	
	Ψ_6	4.6 (6.2)	
	Ψ_7	4.6 (6.2)	
	Ψ_8	9.9 (13.1)	
	Ψ_9	18.3 (21.5)	
			$\Psi_{1,T} S=1, M_z=0\rangle$
			$\frac{1}{\sqrt{2}} \Psi_{1,T} (S=1, M_z=1\rangle + S=1, M_z=-1\rangle)$
			$\frac{1}{\sqrt{2}} \Psi_{1,T} (- S=1, M_z=1\rangle + S=1, M_z=-1\rangle)$
		$\frac{1}{\sqrt{2}} (\Psi_{2,T} + i\Psi_{3,T}) S=1, M_z=1\rangle$	
		$\frac{1}{\sqrt{2}} (\Psi_{2,T} - i\Psi_{3,T}) S=1, M_z=-1\rangle$	
		$\Psi_{2,T} S=1, M_z=0\rangle$	
		$\Psi_{3,T} S=1, M_z=0\rangle$	
		$\frac{1}{2} \Psi_{2,T} (S=1, M_z=1\rangle + S=1, M_z=-1\rangle) - i\frac{1}{2} \Psi_{3,T} (S=1, M_z=1\rangle - S=1, M_z=-1\rangle)$	
		$-\frac{1}{2} \Psi_{2,T} (S=1, M_z=1\rangle - S=1, M_z=-1\rangle) + i\frac{1}{2} \Psi_{3,T} (S=1, M_z=1\rangle + S=1, M_z=-1\rangle)$	

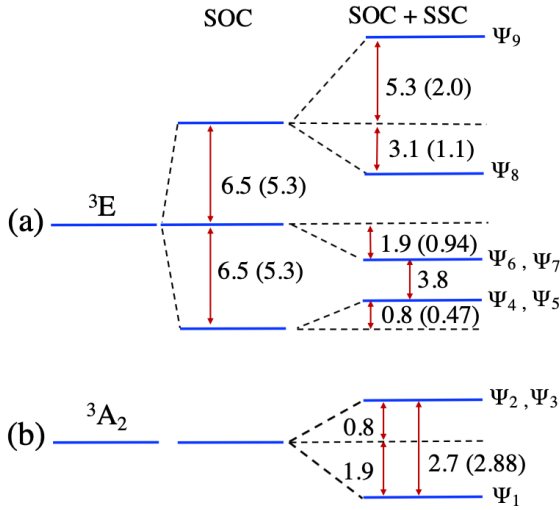


FIG. 5. Schematic diagram of our calculated energy level splitting of (a) the first-excited triplet 3E state and (b) the ground 3A_2 state due to SOC and SSC in units of GHz (for 70-atom cluster). The experimental values⁶⁵ are shown inside parentheses. States $\Psi_{1,\dots,9}$ are defined in Table IV.

and its splitting by higher-order SOC is negligible. However, we find that the SSC splits the 3A_2 state into one lower non-degenerate level with $M_z = 0$ and one higher doubly degenerate level with $M_z = \pm 1$ by -1.9 GHz and 0.8 GHz, respectively. (See the eigenvectors $\Psi_{1,2,3}$ in Table IV.) Therefore, the energy separation between them is about 2.7 GHz, which is in excellent agreement with the experimental value of 2.88 GHz⁶⁵ as well as a previous DFT calculation⁴⁷.

On the other hand, the SOC splits the 3E state into three (degenerate) groups, each of which has eigenvalues of the z component of orbital angular momentum, L_z , of ± 0.46 (± 0.53) for the 70-atom (162-atom) cluster. The separation of the levels is about 6.5 GHz for the 70-atom cluster (Fig. 5) and about 8.1 GHz for the 162-

atom cluster. Our calculated level splitting values show a weak cluster-size dependence and they are somewhat larger than the experimental value of 5.3 GHz⁶⁵. A possible reason for this is the dynamic Jahn-Teller effect^{66,67} and the resulting quenching of SOC (i.e., Ham reduction factor^{37,68,69}) Note that our calculations are done for zero strain without electron-phonon coupling. Quantum-chemistry calculations of electron-phonon coupling and the dynamic Jahn-Teller effect are worth investigating in the future. In addition to the SOC-induced splitting, the SSC further shifts the lowest degenerate level upward by 0.8 GHz (Ψ_4, Ψ_5 in Table IV) and moves the second degenerate level downward by 1.9 GHz (Ψ_6, Ψ_7). In this case, the degeneracy still holds. Interestingly, the amount of the downward level shift is almost twice that of the upward shift. The trend of the level-shift direction as well as the ratio between the downward and upward shift amount, are in good agreement with experiment⁶⁵, although our shifted values are off by a factor of 2 compared to experiment. We also find that the SSC splits the third doubly degenerate level into two separate levels (Ψ_8, Ψ_9): one level shifts downward by 3.1 GHz and the other moves upward by 5.3 GHz. Again, the trend of the level shift agrees with experiment⁶⁵, although the calculated shift amount is greater than experiment by a factor of 2 or 3. This overestimated SSC contribution may partially arise from our first-order perturbation treatment of SSC.

VI. CONCLUSION AND OUTLOOK

We have developed a systematic numerical procedure to compute the electronic structure and magnetic properties of an NV⁻ center defect in diamond clusters, using the (multiconfigurational) quantum chemistry methods, where electron correlation is properly included. We found that the crucial constituent in the procedure is to identify and include extra unoccupied defect orbitals (beyond the four dangling bond orbitals) in the active space. Our

quantum chemistry calculations showed that the first-excited spin-triplet 3E state is separated from the ground state (3A_2) by 1.93-2.14 eV, while the first-excited spin-singlet 1E state is separated from the lower-energy 1A_1 state by 1.07-1.35 eV. In addition, we found that the 3E state is separated from the 1A_1 state by 0.52-0.54 eV. Our calculated triplet-triplet, singlet-singlet, and triplet-singlet excitation energies as well as the ordering of the triplet and singlet states are in good agreement with experiment. We found additional configurations which significantly contribute to the 1E and 1A_1 states, which have not been considered before. Furthermore, SOC and SSC were included in our many-body wave functions, finding that the SSC splits the 3A_2 state by 2.7 GHz and that a combination of the SOC and SSC splits the 3E state into two degenerate levels and two non-degenerate levels. The SSC-induced splitting of the 3A_2 state and the SOC-induced splitting of the 3E state in good agreement with experiment. When both SOC and SSC are included in the 3E state, the calculated trend of the level splitting agree well with experiment and the splitting amount is mostly deviated from experiment by a factor of two.

The numerical procedure that we developed in this work can be applied to other deep defects in wide band-gap semiconducting materials such as group-IV defects and transition-metal defects in diamond or silicon carbide, or rare-earth defects in silicon or complex oxides, as long as a sufficient number of defect-localized orbitals is judiciously chosen for the active space while retaining the defect symmetries and orbital degeneracy as accurately as possible. This procedure may also be extended to obtain radiative transition rates between the states and can be applied to deep defects with external perturbations such as electric fields and strains. Therefore, our findings open a new avenue to be able to screen other defects desirable for specific applications beyond to accurately predict the properties of their excited states.

ACKNOWLEDGMENTS

The authors were supported by the National Science Foundation under a collaborative grant (Grant numbers DMR-1737921 for S.E.E. and K.P. and DMR-1738076 for P.D.). We are grateful to Adam Gali, Kai-Mei Fu, Marcus Doherty, and Audrius Alkauskas for useful comments on the manuscript. The computational support was provided by the Virginia Tech Advanced Research Computing and the Extreme Science and Engineering Discovery Environment (XSEDE) under Project number DMR060009N (K.P.) and Project number PHY180014 (P.D.), which are supported by the National Science Foundation Grant number ACI-1548562.

Appendix A: Procedure of identifying active orbitals and performing CASSCF(6,6)

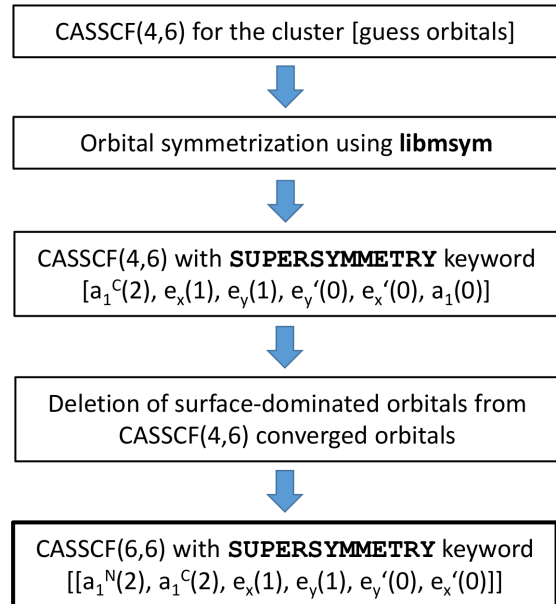


FIG. 6. Schematic diagram of our practical procedure to identify two extra unoccupied defect orbitals and to perform the CASSCF(6,6) calculations of an NV^- center defect in the hydrogen-passivated 70-atom and 162-atom diamond clusters, using `OpenMolcas`. Here initial orbitals in the active space are listed within brackets, where nominal occupation numbers for the spin-triplet ground state are shown inside parentheses. The nominal occupation numbers differ from the actual occupation numbers. The orbitals inside double brackets are final converged orbitals. `libmsym` is an orbital-symmetrization program⁷⁰ and the function of `SUPERSYMMETRY` keyword is defined in the text of the Appendix.

In order to identify extra unoccupied defect orbitals beyond the four dangling bond orbitals as discussed in Section 4, we carry out the following systematic procedure for the 70-atom and 162-atom clusters with the total spin $S = 1$. Figure 6 summarizes the CASSCF procedure using `OpenMolcas`. Note that extra unoccupied defect orbitals cannot be found from the CASSCF(6,4) calculation. The doubly occupied a_1^N orbital is known to have a lower energy than the doubly occupied a_1^C orbital and the former is buried in the bulk valence band. Therefore, excluding the a_1^N orbital, we envision a CASSCF(4,6) calculation where six active orbitals consist of three dangling bond orbitals (a_1^C , e_x , e_y), two unoccupied defect orbitals with E IRRep, and one unoccupied defect orbital with A_1 IRRep. Keeping this in mind, we first perform a CASSCF(4,6) calculation (with state average over six roots) using four active electrons and initial six active orbitals guessed by `OpenMolcas`. Then converged orbitals from the CASSCF(4,6) calculation are fully symmetrized with C_{3v} symmetry, using the `libmsym` program⁷⁰ that is

interfaced with `OpenMolcas`. The `libmsym` program can deal with higher point-group symmetries than twofold symmetry. Now each molecular orbital in the inactive, active and virtual spaces has its own pure IRRep symmetry. Among these symmetrized orbitals, we identify two extra unoccupied orbitals localized near the defect with e_x and e_y symmetries, as well as one unoccupied defect orbital with a_1 symmetry. In order to distinguish these extra orbitals with e_x and e_y symmetries from the singly occupied dangling bond orbitals (e_x and e_y), the former orbitals are referred to as e'_x and e'_y orbitals. Now using these extra three unoccupied defect orbitals as well as the three dangling bond orbitals as initial six active orbitals, we carry out another CASSCF(4,6) calculation with restricted orbital rotations throughout iterations, in other words, orbital rotations (or optimization) are allowed only among the orbitals belonging to the same IRRep. This restriction can be achieved using `SUPERSYMMETRY` keyword in `OpenMolcas` code. The steps of `libmsym` and `SUPERSYMMETRY` are crucial to maintain purely-symmetric orbitals throughout the self-consistent calculations and more importantly to retain the perfect degeneracy of the converged CASSCF energy eigenvalues (the accuracy of ~ 10 neV) belonging to the IRRep E . Such high accuracy is required for an accurate calculation of zero-field splitting induced by SOC. After the second CASSCF(4,6) calculation, the two unoccupied defect orbitals, e'_x and e'_y , remain in the active space.

In our molecular cluster models for an NV^- center,

the hydrogen-passivated surface is artificial since it does not exist in a diamond lattice. Therefore, orbitals localized at the surface are not associated with the defect in a diamond lattice. In order to reduce an effect of such surface-dominated orbitals on the orbital optimization, we remove several tens of surface-dominated orbitals near the active space from the converged orbitals in the second CASSCF(4,6) calculation. More surface orbitals are removed for a larger cluster. After this step, we now carry out a CASSCF(6,6) calculation with `SUPERSYMMETRY` keyword using the identified e'_x and e'_y orbitals (from the CASSCF(4,6) calculation) as well as the four dangling bond orbitals as initial active orbitals. We check that the energy levels (root energies) obtained from the CASSCF(6,6) calculation do not change as the number of removed surface orbitals varies, as long as enough number of surface orbitals are removed near the active space.

The similar procedure to Fig. 6 is carried out for the total spin $S = 0$ with state average over six roots for both 70-atom and 162-atom clusters. Then we perform another CASSCF(6,6) calculation with state average over four roots, using the converged CASSCF(6,6) orbitals, in order to retain the perfect degeneracy of the CASSCF energy eigenvalues in the E IRRep and the localization of the active orbitals. We emphasize that the orbital symmetrization is more important for the spin-singlet states than for the spin-triplet states.

* Current Address: The Ames Laboratory, U.S. Department of Energy, Iowa State University, Ames, IA 50011-3020, USA

† kyungwha@vt.edu (corresponding author)

¹ J. R. Maze, P. L. Stanwix, J. S. Hodges, S. Hong, J. M. Taylor, P. Cappellaro, L. Jiang, M. V. Gurudev Dutt, E. Togan, A. S. Zibrov, A. Yacoby, R. L. Walsworth, and M. D. Lukin. Nanoscale magnetic sensing with an individual electronic spin in diamond. *Nature*, 455(7213):644–647, Oct 2008.

² Gopalakrishnan Balasubramanian, I. Y. Chan, Roman Kolesov, Mohannad Al-Hmoud, Julia Tisler, Chang Shin, Changdong Kim, Aleksander Wojcik, Philip R. Hemmer, Anke Krueger, Tobias Hanke, Alfred Leitenstorfer, Rudolf Bratschitsch, Fedor Jelezko, and Jörg Wrachtrup. Nanoscale imaging magnetometry with diamond spins under ambient conditions. *Nature*, 455(7213):648–651, Oct 2008.

³ B. Hensen, H. Bernien, A. E. Dréau, A. Reiserer, N. Kalb, M. S. Blok, J. Ruitenbergh, R. F. L. Vermeulen, R. N. Schouten, C. Abellán, W. Amaya, V. Pruneri, M. W. Mitchell, M. Markham, D. J. Twitchen, D. Elkouss, S. Wehner, T. H. Taminiau, and R. Hanson. Loophole-free Bell inequality violation using electron spins separated by 1.3 kilometres. *Nature*, 526(7575):682–686, Oct 2015.

⁴ T. H. Taminiau, J. Cramer, T. van der Sar, V. V. Dobrovitski, and R. Hanson. Universal control and error correction in multi-qubit spin registers in diamond. *Nature Nanotechnology*, 9(3):171–176, Mar 2014.

⁵ G. Waldherr, Y. Wang, S. Zaiser, M. Jamali, T. Schulte-Herbrüggen, H. Abe, T. Ohshima, J. Isoya, J. F. Du, P. Neumann, and J. Wrachtrup. Quantum error correction in a solid-state hybrid spin register. *Nature*, 506(7487):204–207, Feb 2014.

⁶ Lucio Robledo, Lilian Childress, Hannes Bernien, Bas Hensen, Paul F. A. Alkemade, and Ronald Hanson. High-fidelity projective read-out of a solid-state spin quantum register. *Nature*, 477(7366):574–578, Sep 2011.

⁷ Peter C. Humphreys, Norbert Kalb, Jaco P. J. Morits, Raymond N. Schouten, Raymond F. L. Vermeulen, Daniel J. Twitchen, Matthew Markham, and Ronald Hanson. Deterministic delivery of remote entanglement on a quantum network. *Nature*, 558(7709):268–273, Jun 2018.

⁸ A. Jarmola, V. M. Acosta, K. Jensen, S. Chemerisov, and D. Budker. Temperature- and magnetic-field-dependent longitudinal spin relaxation in nitrogen-vacancy ensembles in diamond. *Phys. Rev. Lett.*, 108:197601, May 2012.

⁹ T. Astner, J. Gugler, A. Angerer, S. Wald, S. Putz, N. J. Mauser, M. Trupke, H. Sumiya, S. Onoda, J. Isoya, J. Schmiedmayer, P. Mohn, and J. Majer. Solid-state electron spin lifetime limited by phononic vacuum modes. *Nature Materials*, 17(4):313–317, Apr 2018.

¹⁰ Nan Zhao, Jan Honert, Bernhard Schmid, Michael Klas, Junichi Isoya, Matthew Markham, Daniel Twitchen, Fedor Jelezko, Ren-Bao Liu, Helmut Fedder, and Jörg Wrachtrup. Sensing single remote nuclear spins. *Nature*

- Nanotechnology*, 7(10):657–662, Oct 2012.
- 11 N. Bar-Gill, L. M. Pham, A. Jarmola, D. Budker, and R. L. Walsworth. Solid-state electronic spin coherence time approaching one second. *Nature Communications*, 4(1):1743, Apr 2013.
 - 12 David D. Awschalom, Ronald Hanson, Jörg Wrachtrup, and Brian B. Zhou. Quantum technologies with optically interfaced solid-state spins. *Nature Photonics*, 12(9):516–527, Sep 2018.
 - 13 Lee C. Bassett, Audrius Alkauskas, Annemarie L. Exarhos, and Kai-Mei C. Fu. Quantum defects by design. *Nanophotonics*, 8(11):1867 – 1888, 2019.
 - 14 Christopher G. Yale, Bob B. Buckley, David J. Christle, Guido Burkard, F. Joseph Heremans, Lee C. Bassett, and David D. Awschalom. All-optical control of a solid-state spin using coherent dark states. *Proceedings of the National Academy of Sciences*, 110(19):7595–7600, 2013.
 - 15 G. D. Fuchs, V. V. Dobrovitski, D. M. Toyli, F. J. Heremans, and D. D. Awschalom. Gigahertz dynamics of a strongly driven single quantum spin. *Science*, 326(5959):1520–1522, 2009.
 - 16 William F. Koehl, Bob B. Buckley, F. Joseph Heremans, Greg Calusine, and David D. Awschalom. Room temperature coherent control of defect spin qubits in silicon carbide. *Nature*, 479(7371):84–87, Nov 2011.
 - 17 Matthias Widmann, Sang-Yun Lee, Torsten Rendler, Nguyen Tien Son, Helmut Fedder, Seoyoung Paik, Li-Ping Yang, Nan Zhao, Sen Yang, Ian Booker, Andrej Denisenko, Mohammad Jamali, S. Ali Momenzadeh, Ilja Gerhardt, Takeshi Ohshima, Adam Gali, Erik Janzén, and Jörg Wrachtrup. Coherent control of single spins in silicon carbide at room temperature. *Nature Materials*, 14(2):164–168, Feb 2015.
 - 18 Ö. O. Soykal, Pratibha Dev, and Sophia E. Economou. Silicon vacancy center in 4h-sic: Electronic structure and spin-photon interfaces. *Phys. Rev. B*, 93:081207(R), Feb 2016.
 - 19 Michel Bockstedte, Felix Schütz, Thomas Garratt, Viktor Ivády, and Adam Gali. Ab initio description of highly correlated states in defects for realizing quantum bits. *npj Quantum Materials*, 3(1):31, Jun 2018.
 - 20 Roland Nagy, Matthias Niethammer, Matthias Widmann, Yu-Chen Chen, Péter Udvarhelyi, Cristian Bonato, Jawad Ul Hassan, Robin Karhu, Ivan G. Ivanov, Nguyen Tien Son, Jeronimo R. Maze, Takeshi Ohshima, Öney O. Soykal, Ádám Gali, Sang-Yun Lee, Florian Kaiser, and Jörg Wrachtrup. High-fidelity spin and optical control of single silicon-vacancy centres in silicon carbide. *Nature Communications*, 10(1):1954, Apr 2019.
 - 21 A. M. Edmonds, M. E. Newton, P. M. Martineau, D. J. Twitchen, and S. D. Williams. Electron paramagnetic resonance studies of silicon-related defects in diamond. *Phys. Rev. B*, 77:245205, Jun 2008.
 - 22 Adam Gali and Jeronimo R. Maze. Ab initio study of the split silicon-vacancy defect in diamond: Electronic structure and related properties. *Phys. Rev. B*, 88:235205, Dec 2013.
 - 23 Benjamin Pingault, David-Dominik Jarausch, Christian Hepp, Lina Klintberg, Jonas N. Becker, Matthew Markham, Christoph Becher, and Mete Atatüre. Coherent control of the silicon-vacancy spin in diamond. *Nature Communications*, 8(1):15579, May 2017.
 - 24 Brendon C. Rose, Ding Huang, Zi-Huai Zhang, Paul Stevenson, Alexei M. Tyryshkin, Sorawis Sangtawesin, Srikanth Srinivasan, Lorne Loudin, Matthew L. Markham, Andrew M. Edmonds, Daniel J. Twitchen, Stephen A. Lyon, and Nathalie P. de Leon. Observation of an environmentally insensitive solid-state spin defect in diamond. *Science*, 361(6397):60–63, 2018.
 - 25 He Ma, Marco Govoni, and Giulia Galli. Quantum simulations of materials on near-term quantum computers. *npj Computational Materials*, 6(1):85, Jul 2020.
 - 26 Chunming Yin, Milos Rancic, Gabriele G. de Boo, Nikolas Stavrias, Jeffrey C. McCallum, Matthew J. Sellars, and Sven Rogge. Optical addressing of an individual erbium ion in silicon. *Nature*, 497(7447):91–94, May 2013.
 - 27 Thomas Kornher, Da-Wu Xiao, Kangwei Xia, Fiammetta Sardi, Nan Zhao, Roman Kolesov, and Jörg Wrachtrup. Sensing individual nuclear spins with a single rare-earth electron spin. *Phys. Rev. Lett.*, 124:170402, Apr 2020.
 - 28 Adam Gali, Maria Fyta, and Efthimios Kaxiras. Ab initio supercell calculations on nitrogen-vacancy center in diamond: Electronic structure and hyperfine tensors. *Phys. Rev. B*, 77:155206, Apr 2008.
 - 29 A. Lenef and S. C. Rand. Electronic structure of the n-v center in diamond: Theory. *Phys. Rev. B*, 53:13441–13455, May 1996.
 - 30 N. B. Manson, J. P. Harrison, and M. J. Sellars. Nitrogen-vacancy center in diamond: Model of the electronic structure and associated dynamics. *Phys. Rev. B*, 74:104303, Sep 2006.
 - 31 L J Rogers, S Armstrong, M J Sellars, and N B Manson. Infrared emission of the NV centre in diamond: Zeeman and uniaxial stress studies. *New Journal of Physics*, 10(10):103024, oct 2008.
 - 32 V. M. Acosta, A. Jarmola, E. Bauch, and D. Budker. Optical properties of the nitrogen-vacancy singlet levels in diamond. *Phys. Rev. B*, 82:201202(R), Nov 2010.
 - 33 A. Batalov, C. Zierl, T. Gaebel, P. Neumann, I.-Y. Chan, G. Balasubramanian, P. R. Hemmer, F. Jelezko, and J. Wrachtrup. Temporal coherence of photons emitted by single nitrogen-vacancy defect centers in diamond using optical rabi-oscillations. *Phys. Rev. Lett.*, 100:077401, Feb 2008.
 - 34 D. M. Toyli, D. J. Christle, A. Alkauskas, B. B. Buckley, C. G. Van de Walle, and D. D. Awschalom. Measurement and control of single nitrogen-vacancy center spins above 600 k. *Phys. Rev. X*, 2:031001, Jul 2012.
 - 35 P. Kehayias, M. W. Doherty, D. English, R. Fischer, A. Jarmola, K. Jensen, N. Leefer, P. Hemmer, N. B. Manson, and D. Budker. Infrared absorption band and vibronic structure of the nitrogen-vacancy center in diamond. *Phys. Rev. B*, 88:165202, Oct 2013.
 - 36 M. L. Goldman, A. Sipahigil, M. W. Doherty, N. Y. Yao, S. D. Bennett, M. Markham, D. J. Twitchen, N. B. Manson, A. Kubanek, and M. D. Lukin. Phonon-induced population dynamics and intersystem crossing in nitrogen-vacancy centers. *Phys. Rev. Lett.*, 114:145502, Apr 2015.
 - 37 M. L. Goldman, M. W. Doherty, A. Sipahigil, N. Y. Yao, S. D. Bennett, N. B. Manson, A. Kubanek, and M. D. Lukin. Erratum: State-selective intersystem crossing in nitrogen-vacancy centers [phys. rev. b 91, 165201 (2015)]. *Phys. Rev. B*, 96:039905(E), Jul 2017.
 - 38 Paul Delaney, James C. Greer, and J. Andreas Larsson. Spin-polarization mechanisms of the nitrogen-vacancy center in diamond. *Nano Letters*, 10(2):610–614, 2010.
 - 39 J. P. Goss, R. Jones, S. J. Breuer, P. R. Briddon, and S. Öberg. The twelve-line 1.682 eV luminescence center

- in diamond and the vacancy-silicon complex. *Phys. Rev. Lett.*, 77:3041–3044, Sep 1996.
- 40 A. S. Zyubin, A. M. Mebel, M. Hayashi, H. C. Chang, and S. H. Lin. Quantum chemical modeling of photoadsorption properties of the nitrogen-vacancy point defect in diamond. *Journal of Computational Chemistry*, 30(1):119–131, 2009.
- 41 Chih-Kai Lin, Yi-Hsieh Wang, Huan-Cheng Chang, M. Hayashi, and S. H. Lin. One- and two-photon absorption properties of diamond nitrogen-vacancy defect centers: A theoretical study. *The Journal of Chemical Physics*, 129(12):124714, 2008.
- 42 G. Davies, M. F. Hamer, and William Charles Price. Optical studies of the 1.945 eV vibronic band in diamond. *Proceedings of the Royal Society of London. A. Mathematical and Physical Sciences*, 348(1653):285–298, 1976.
- 43 Yuchen Ma, Michael Rohlfing, and Adam Gali. Excited states of the negatively charged nitrogen-vacancy color center in diamond. *Phys. Rev. B*, 81:041204(R), Jan 2010.
- 44 SangKook Choi, Manish Jain, and Steven G. Louie. Mechanism for optical initialization of spin in nv^- center in diamond. *Phys. Rev. B*, 86:041202(R), Jul 2012.
- 45 John P. Perdew, Kieron Burke, and Yue Wang. Generalized gradient approximation for the exchange-correlation hole of a many-electron system. *Phys. Rev. B*, 54:16533–16539, Dec 1996.
- 46 P Giannozzi et al. Advanced capabilities for materials modelling with quantum espresso. *Journal of Physics: Condensed Matter*, 29(46):465901, 2017.
- 47 Viktor Ivády, Tamás Simon, Jeronimo R. Maze, I. A. Abrikosov, and Adam Gali. Pressure and temperature dependence of the zero-field splitting in the ground state of nv centers in diamond: A first-principles study. *Phys. Rev. B*, 90:235205, Dec 2014.
- 48 Björn O Roos, Roland Lindh, Per Åke Malmqvist, Valera Veryazov, and Per-Olof Widmark. *Multiconfigurational quantum chemistry*. John Wiley & Sons, 2016.
- 49 Fdez. Galván Ignacio et al. Openmolcas: From source code to insight. *Journal of Chemical Theory and Computation*, 15(11):5925–5964, 2019.
- 50 Frank Neese. Software update: the orca program system, version 4.0. *WIREs Computational Molecular Science*, 8(1):e1327, 2018.
- 51 Frank Neese. The orca program system. *WIREs Computational Molecular Science*, 2(1):73–78, 2012.
- 52 Thom H. Dunning. Gaussian basis sets for use in correlated molecular calculations. i. the atoms boron through neon and hydrogen. *The Journal of Chemical Physics*, 90(2):1007–1023, 1989.
- 53 W. A de Jong, R. J. Harrison, and D. A. Dixon. Parallel douglas-kroll energy and gradients in nwchem: Estimating scalar relativistic effects using douglas-kroll contracted basis sets. *The Journal of Chemical Physics*, 114(1):48–53, 2001.
- 54 J R Maze, A Gali, E Togan, Y Chu, A Trifonov, E Kaxiras, and M D Lukin. Properties of nitrogen-vacancy centers in diamond: the group theoretic approach. *New Journal of Physics*, 13(2):025025, feb 2011.
- 55 M W Doherty, N B Manson, P Delaney, and L C L Hollenberg. The negatively charged nitrogen-vacancy centre in diamond: the electronic solution. *New Journal of Physics*, 13(2):025019, feb 2011.
- 56 Goran Kovačević and Valera Veryazov. Luscus: molecular viewer and editor for molcas. *Journal of Cheminformatics*, 7(1):16, Apr 2015.
- 57 Bernd A. Hess, Christel M. Marian, Ulf Wahlgren, and Odd Gropen. A mean-field spin-orbit method applicable to correlated wavefunctions. *Chem. Phys. Lett.*, 251(5):365–371, 1996.
- 58 Per Åke Malmqvist, Björn O Roos, and Bernd Schimmelpfennig. The restricted active space (ras) state interaction approach with spin-orbit coupling. *Chem. Phys. Lett.*, 357(3-4):230–240, 2002.
- 59 Frank Neese. Importance of direct spin-spin coupling and spin-flip excitations for the zero-field splittings of transition metal complexes: a case study. *Journal of the American Chemical Society*, 128(31):10213–10222, 2006.
- 60 J. P. Goss, R. Jones, S. J. Breuer, P. R. Briddon, and S. Öberg. The twelve-line 1.682 eV luminescence center in diamond and the vacancy-silicon complex. *Phys. Rev. Lett.*, 77:3041–3044, Sep 1996.
- 61 Gergely Barcza, Viktor Ivády, Tibor Szilvási, Márton Vörös, Libor Veis, Ádám Gali, and Örs Legeza. Dmrg on top of plane-wave kohn-sham orbitals: case study of defected boron nitride. *arXiv*, page 2006.04557, 2020.
- 62 J. A. Larsson and P. Delaney. Electronic structure of the nitrogen-vacancy center in diamond from first-principles theory. *Phys. Rev. B*, 77:165201, Apr 2008.
- 63 Ádám Gali. Ab initio theory of the nitrogen-vacancy center in diamond. *Nanophotonics*, 8(11):1907–1943, 2019.
- 64 Ph Tamarat, N B Manson, J P Harrison, R L McMurtrie, A Nizovtsev, C Santori, R G Beausoleil, P Neumann, T Gaebel, F Jelezko, P Hemmer, and J Wrachtrup. Spin-flip and spin-conserving optical transitions of the nitrogen-vacancy centre in diamond. *New Journal of Physics*, 10(4):045004, apr 2008.
- 65 A. Batalov, V. Jacques, F. Kaiser, P. Siyushev, P. Neumann, L. J. Rogers, R. L. McMurtrie, N. B. Manson, F. Jelezko, and J. Wrachtrup. Low temperature studies of the excited-state structure of negatively charged nitrogen-vacancy color centers in diamond. *Phys. Rev. Lett.*, 102:195506, May 2009.
- 66 Kai-Mei C. Fu, Charles Santori, Paul E. Barclay, Lachlan J. Rogers, Neil B. Manson, and Raymond G. Beausoleil. Observation of the dynamic jahn-teller effect in the excited states of nitrogen-vacancy centers in diamond. *Phys. Rev. Lett.*, 103:256404, Dec 2009.
- 67 Tesfaye A. Abtey, Y. Y. Sun, Bi-Ching Shih, Pratibha Dev, S. B. Zhang, and Peihong Zhang. Dynamic jahn-teller effect in the nv^- center in diamond. *Phys. Rev. Lett.*, 107:146403, Sep 2011.
- 68 Frank S. Ham. Effect of linear jahn-teller coupling on paramagnetic resonance in a 2e state. *Phys. Rev.*, 166:307–321, Feb 1968.
- 69 Gergő Thiering and Adam Gali. Ab initio calculation of spin-orbit coupling for an nv center in diamond exhibiting dynamic jahn-teller effect. *Phys. Rev. B*, 96:081115(R), Aug 2017.
- 70 Johansson Marcus and Valera Veryazov. Automatic procedure for generating symmetry adapted wavefunctions. *Journal of cheminformatics*, 9:8, 2017.